AD-A163 034 ELECTROMAGNETIC SCATTERING PROPERTIES OF FINITE CYLINDERS AND SPHEROIDS(U) DREXEL UNIV PHILADELPHIA PA L D COHEN ET AL NOV 85 CRDC-CR-85041 DAAK11-81-K-0003 1/1

UNCLASSIFIED F/G 20/6 NL

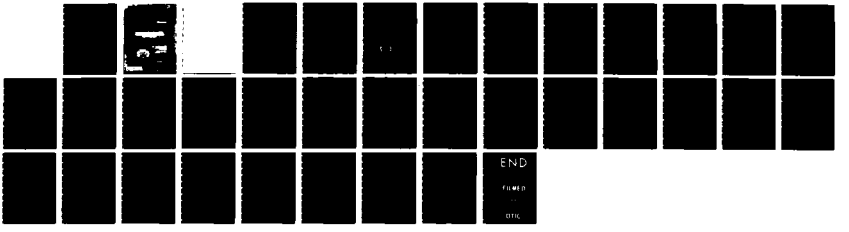

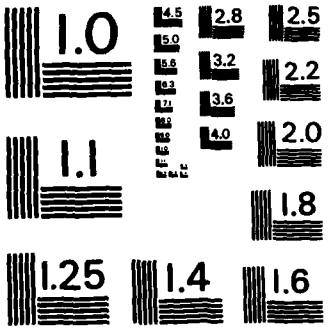

MICROCOPY RESOLUTION TEST CHART
NATIONAL BUREAU OF STANDARDS-1963-A

CHEMICAL
RESEARCH &
DEVELOPMENT
CENTER

UNCLASSIFIED
SECURITY CLASSIFICATION OF THIS PAGE

AD-A163 034

REPORT DOCUMENTATION PAGE

1a. REPORT SECURITY CLASSIFICATION UNCLASSIFIED	1b. RESTRICTIVE MARKINGS
2a. SECURITY CLASSIFICATION AUTHORITY	3. DISTRIBUTION/AVAILABILITY OF REPORT Approved for public release; distribution is unlimited.
2b. DECLASSIFICATION/DOWNGRADING SCHEDULE	
4. PERFORMING ORGANIZATION REPORT NUMBER(S) CRDC-CR-85041	5. MONITORING ORGANIZATION REPORT NUMBER(S)
6a. NAME OF PERFORMING ORGANIZATION Drexel University 6b. OFFICE SYMBOL (If applicable)	7a. NAME OF MONITORING ORGANIZATION Office of Naval Research
6c. ADDRESS (City, State, and ZIP Code) 32nd & Chestnut Streets Philadelphia, PA 19104	7b. ADDRESS (City, State, and ZIP Code) 2100 Pennsylvania Avenue, NW Washington, DC 20037
8a. NAME OF FUNDING/SPONSORING ORGANIZATION CRDC 8b. OFFICE SYMBOL (If applicable) SMCCR-RSP-B	9. PROCUREMENT INSTRUMENT IDENTIFICATION NUMBER DAAK11-81-K-0003
8c. ADDRESS (City, State, and ZIP Code) Aberdeen Proving Ground, MD 21010-5423	10. SOURCE OF FUNDING NUMBERS PROGRAM ELEMENT NO. / PROJECT NO. 1L161102 / TASK NO. A71A / WORK UNIT ACCESSION NO.

11. TITLE (Include Security Classification)
Electromagnetic Scattering Properties of Finite Cylinders and Spheroids

12. PERSONAL AUTHOR(S)
Cohen, Leonard D., Haracz, Richard D., and Cohen, Ariel

13a. TYPE OF REPORT	13b. TIME COVERED	14. DATE OF REPORT (Year, Month, Day)	15. PAGE COUNT
Contractor	FROM 81 Jun TO 84 Aug	1985 November	33

16. SUPPLEMENTARY NOTATION
COR: Dr. E. Steubing, SMCCR-RSP-B, (301)671-3089

17. COSATI CODES			18. SUBJECT TERMS (Continue on reverse if necessary and identify by block number)
FIELD	GROUP	SUB-GROUP	
20	03		Light scattering, Scattering by Ellipsoids, Scattering by Cylinders, Multiple Scattering
20	06		

19. ABSTRACT (Continue on reverse if necessary and identify by block number)

The perturbation theory suggested by Shifrin is applied through the second order to the scattering of light from dielectric spheroids and finite cylinders.

Double scattering events involving long cylindrical particles are discussed.

Comparisons between experimental and theoretical scattering from long brass and copper cylinders are discussed also.

20. DISTRIBUTION/AVAILABILITY OF ABSTRACT	21. ABSTRACT SECURITY CLASSIFICATION
☒ UNCLASSIFIED/UNLIMITED ☐ SAME AS RPT. ☐ DTIC USERS	UNCLASSIFIED
22a. NAME OF RESPONSIBLE INDIVIDUAL TIMOTHY E. HAMPTON	22b. TELEPHONE (Include Area Code) (301) 671-2914
	22c. OFFICE SYMBOL SMCCR-SPD-R

DD FORM 1473, 84 MAR — 83 APR edition may be used until exhausted. All other editions are obsolete.

SECURITY CLASSIFICATION OF THIS PAGE
UNCLASSIFIED

PREFACE

The work described in this report was authorized under Project No. 1L161102A71A and Contract No. DAAK11-81-K-0003. This work was started in June 1981 and completed in August 1984.

The use of trade names or manufacturers' names in this report does not constitute endorsement of any commercial products. This report may not be cited for purposes of advertisement.

This report has been approved for release to the public.

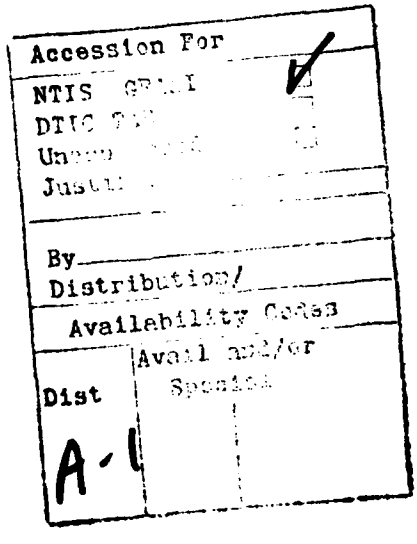

CONTENTS

LIST OF FIGURES

ELECTROMAGNETIC SCATTERING PROPERTIES OF FINITE CYLINDERS AND SPHEROIDS

1. INTRODUCTION

This report describes the work done and the progress made in determining the electromagnetic (EM) scattering properties of small non-spherical particles. In particular, the purpose of the contract was to extend and evaluate the modified Shifrin integro-differential equation solution[1] to the EM scattering by finite cylinders and spheroids. These solutions are then used in formulating an analytic tool for the investigation of multiple scattering by non-spherical particles.

The solutions for scattering by finite cylinders and spheroids developed by C. Acquista[2] have been generalized to allow for arbitrary polarization of the incident EM radiation, polarization scattered directions[3] and arbitrary orientations of the scattering particles. A number of comparisons with "exact" theory[4] have been developed to determine the range of applicability of the modified Shifrin[5] approach. We have, in addition, developed internal electrostatic solutions for short cylinders so that the Shifrin method[5] may be used to compute the scattering by such particles.

A very detailed, general, double scattering problem has been analyzed and computations performed for double scattering from randomly oriented, infinitely long cylinders. The problem of double scattering from finite cylinders and spheroids has been analyzed; however, the programming of the solution was not completed.

A comparison of the results of scattering experiments conducted at Fairleigh Dickinson University with calculations from our infinite cylinder code has yielded excellent agreement[6].

2. PERTURBATION THEORY FOR SCATTERING FROM DIELECTRIC SPHEROIDS AND SHORT CYLINDERS

The solution of Maxwell's equation for the scattering of a plane wave from an isotropic and non-magnetic medium can be expressed by the integro-differential equation

$$\vec{E}(\vec{r}) = \vec{E}_o \exp(i\vec{k}_o\cdot\vec{r}) + \nabla x\, \nabla x \int d^3r' \left(\frac{m^2-1}{4\pi}\right) \frac{\exp(ik_o|\vec{r}-\vec{r}'|)}{|\vec{r}-\vec{r}'|} \vec{E}(\vec{r}') - (m^2-1)\vec{E}(\vec{r}) \qquad (1)$$

where $\vec{E}(\vec{r})$ is the electric field far from the scattering medium, k_o is the propagation vector of the incident wave, and m is the index of refraction of the scattering medium. By expanding the $\nabla x \nabla x$ term by vector identities this equation reduces to

$$\vec{E}(\vec{r}) = \vec{E}_o \exp(i\vec{k}_o \cdot \vec{r}) + (\text{grad div} + k_o^2) \int d^3r' \frac{\exp(ik_o|r-r'|)}{|\vec{r}-\vec{r}'|} \left(\frac{m^2-1}{4\pi}\right) E(r') \quad (2)$$

The Shifrin[5] approach to solve this equation is to estimate the $\vec{E}$ field inside the target medium and use this as the start of an iteractive approach. In fact, in the Rayleigh-Gans-Rocard approximation one uses the external plane wave for the internal field. Acquista's extension[2] of Shifrin's approximation[5] begins with a more realistic choice for the lowest-order approximation in the internal field, namely, the internal solution for an infinite dielectric cylinder in uniform electrostatic field. We adopt this general approach in our work; however, we first need to modify the approach for the case when the light is incident on the cylinder from an arbitrary direction. The solution inside the cylinder is taken to be

$$\vec{E}_i(\vec{r}') = A_{ij} \vec{E}_{effj}(\vec{r}') \quad (3)$$

where E_{eff} is the effective polarizing field inside the cylinder. The polarization matrix is

$$A = \begin{pmatrix} a_{TE} & 0 & 0 \\ 0 & a_{TE} & 0 \\ 0 & 0 & a_{TM} \end{pmatrix} \quad (4)$$

The first-order iterate solution is found to be

$$\vec{E}^{(1)}_{eff}(\vec{r}) = \frac{\exp(ik_o r)}{r} k_o^2 u(k_o\hat{r}-k_o)[(E_{oxl}\hat{i}_1 + E_{oyl}\hat{j}_1) A_{TE} + E_{ozl}\hat{k}_1 A_{TM}]_\perp \quad (5)$$

for the electric field in the far field. The derivation of this equation is detailed in Reference 3. Here $\vec{k}_o$ is the propagation vector of the incident wave, and the subscript $\perp$ means only the portion of the vector perpendicular to the detector direction is to be taken. The pupil function u is the Fourier transform of

$$U(r) = \begin{cases} 1 \text{ inside the cylinder} \\ 0 \text{ outside the cylinder} \end{cases}$$

$$u(x) = \int d^3r'\, U(\vec{r}')\, \exp(i\vec{X}\cdot\vec{r}')$$

$$= \frac{2\pi a^2 h \sin(\chi_{\parallel} h/2) J_1(\chi_{\perp} a)}{(\chi_{\parallel} h/2)(\chi_{\perp} a)} \tag{6}$$

where a is the radius of the cylinder, h is the length, $\vec{\chi}=k\hat{r}-\vec{k}$, and $\parallel$ and $\perp$ refer to the cylinder axis. (see Figure 1 of Reference 3).

The second-order approximation is found to be[4]

$$\vec{E}^{(2)}(\vec{r}) = \frac{2}{(2\pi)^2} \int d^3r'\, \frac{u(\vec{p}+k_o\hat{r})}{p^2-k_o^2}\, u(-\vec{p}-\vec{k}_o) \cdot \left[\left(\frac{p^2+k_o^2}{2}\right)\vec{F}_{\perp} - (\vec{p}\cdot\vec{F})\vec{P}_{\perp}\right] \tag{7}$$

where the vector $\vec{F}$ is defined as

$$\vec{F} = a_{TM}^2(E_{oxl}\hat{i}_1 + E_{oyl}\hat{j}_1) + a_{TM}^2 F_{ozl}\hat{k}_1$$

$$= a_{TE}^2 \vec{F}_{TE} + a_{TM}^2 \vec{F}_{TM} \tag{8}$$

The exact determination of the polarization matrix A is found by solving the electrostatic problem for a dielectric finite cylinder in a constant electric field. This problem does not admit a closed analytic solution. We have shown, however, that by using the infinite cylinder solution as our internal trial function, the iteration procedure converges by second order for aspect ratios ranging from infinity to approximately 20. For this range, the polarization matrix seems to vary only slightly as is shown in Reference 3.

Rewriting the first-order contribution to the electric field we get

$$\vec{E}_{sc}(\vec{r}) \approx \vec{E}^{(1)}(r) = \frac{\exp(i\vec{k}_o\cdot\vec{r})}{r}\, k_o^2 u(k_o\hat{r}-\hat{k}_o) \left(\frac{m^2-1}{4\pi}\right)(\vec{A}_1)_{\perp} \tag{9}$$

where $\vec{A}_1 = \frac{2}{m^2+1}(E_{oxl}\hat{i}_1 + E_{oyl}\hat{j}_1) + E_{ozl}\hat{k}_1$.

$\vec{A}_1$ needs to be expressed in the detector frame (Figure 2 of Reference 3) and we need the portion of $\vec{A}_1$ perpendicular to the detector.

$$(A_1)_\perp = E_o\Big[(\cos\theta\cos\phi,\ \sin\psi\cos\beta/2 - \cos\theta\sin\phi,\ \cos\psi)\frac{2}{m^2+1} - \sin\theta\sin\beta/2\sin\psi\Big]\hat{i} + E_1(\sin\phi,\ \sin\psi\cos\beta/2 + \cos\phi,\ \cos\psi)\frac{2}{m^2+1}\hat{j} \quad (10)$$

The intensity for an electric field polarized in both the initial and final state is defined as

$$I = \frac{k_o^2 r^2}{E_o^2}\left|\vec{E}_{sc}\cdot\hat{\ell}\right|^2 \quad (11)$$

where $\vec{E}_{sc} \approx \vec{E}^{(1)}$ in first order, and $\hat{\ell}$ is a unit vector in the direction of the final state of polarization.

Figure 3 of Reference 3 shows the intensity $I_{||}$ for scattering from an infinite cylinder. The solid curve is computed from first order and the crosses(x) are the result of the exact infinite cylinder computations. It is shown in Reference 3 that this excellent agreement is a consequence of the fact that the first-order theory becomes analytically equal to the exact infinite cylinder results in the limit of the height of the cylinder $h \to \infty$.

Since our goal is to be able to calculate the effect of multiple scattering, we investigated the range of cylinder parameters for which the first-order solutions, which are analytical solutions, converged. Convergence was assumed when the second-order iteration differed from the first order by less than 1%. The rationale for this approach is that the first-order solution requires far less than 1 second to compute an entire scattering distribution, whereas the second-order calculation requires about 20 minutes from the same distribution on the Perkin Elmer 3230. In multiple scattering where the scattering geometry is severely complicated, the combination of the geometry and the second-order calculations would make the computations impractical.

The results of our investigation show that the first order is within 1% of the second order as long as the aspect ratio is 20 or greater, and the phase shift $\delta = 4\pi|m-1|a/\lambda$ is less than 2.

The scattering cone, characteristic of infinite cylinders, is shown to diffuse as the aspect ratio decreases (see Figures 4, 5, 6 and 7 of Reference 3).

3. SHORT DIELECTRIC CYLINDERS

The next step in our program involved the study of short cylinders, with aspect ratios near unity. The Shifrin perturbation theory[5] relies on a reasonably accurate determination of the electrostatic polarization matrix. Though known for the infinite cylinder which we have shown works reasonably well for cylinders down to aspect ratios of 20, it is not available for finite short cylinders. We have used a method for finding A by a technique outlined in a book by van Bladel[7]

The electrostatic potential $\phi(r_o)$ inside the cylinder is related to the surface potential as

$$m^2\,\phi(\vec{r}_o) = \phi_o(\vec{r}_o) - \frac{m^2-1}{4\pi}\oint \phi(\vec{r})\,\frac{\partial}{\partial n}\left|\frac{1}{|r-r_o|}\right| ds \qquad (12)$$

where ϕ_o is the ambient potential, the integral is over the cylinder surface, and $\partial/\partial n$ is the outward normal gradient to the surface. It follows that the electric field inside the cylinder is

$$m^2\,\vec{E}(\vec{r}_o) = \vec{E}_o + \frac{m^2-1}{4\pi}\oint \phi(\vec{r})\nabla\cdot\left[\frac{\partial}{\partial n}\left|\frac{1}{r-r_o}\right|\right] ds \qquad (13)$$

where $\vec{E}_o$ is the ambient electrostatic field. This internal field is related to the electrostatic polarization matrix as

$$E_i(\vec{r}') = A_{ij}\,E_{oj}\exp(ik_o r')$$

and we are led to the following equation for the matrix elements:

$$(m^2 a_i - 1)\,E_{oi} = \frac{m^2-1}{4\pi}\oint_S \phi(\vec{r})\,\frac{\partial}{\partial n}\left[\frac{(\vec{r}-\vec{r}_o)i}{|\vec{r}-\vec{r}_o|^3}\right] ds \qquad (14)$$

where $a_{TE} = a_1 n = a_2$ and $a_{TM} = a_3$.

Therefore, the matrix A is known if we know the surface potential, ϕ and it is determined from the equation

$$\phi(\vec{r}_s) = \frac{2}{m^2+1}\,\phi_o(\vec{r}_s) - \frac{m^2-1}{m^2+1} - \frac{1}{2\pi}\oint \phi(r)\,\frac{\partial}{\partial n}\left|\frac{1}{\vec{r}-\vec{r}_s}\right| ds \qquad (15)$$

where $\vec{r}_s$ is on the cylindrical surface. We solve this equation by an iteration process starting with $\phi = \phi_o$ as the first guess. Convergence occurs rapidly for an index of refraction of 1.33 where only two iterations are necessary.

The results for the elements a_{TE} and a_{TM} are given in Figure 7 of Reference 4 for aspect ratios h/2a = 1/2, 1 and 5. The values are given along the symmetry axis, but they are similar along a perpendicular axis.

It is observed that for an aspect ratio of 5, the elements are quite constant in the central region of the cylinder with values near those for an infinite cylinder. The values of the elements decrease near the ends. The same general variation occurs for the other aspects ratios.

4. THE DIELECTRIC SPHEROID

The dielectric spheroid provides us with one of the very few cases for which exact solutions exist;[8] and thus allows us to evaluate properly the accuracy of the Shifrin approach[5] and the range of convergence of the expansion. For the spheroid, the pupil function u is well known, and it has the forms

$$U(\vec{p}) = V f\left\{ a[p^2 - \epsilon^2 p_\perp^2] \right\} \qquad \text{prolate}$$

$$U(\vec{p}) = V f\left\{ a[p^2 - \epsilon^2 p_{||}^2] \right\} \qquad \text{oblate} \tag{16}$$

where $p_\perp$ and $p_{||}$ are the components of $\vec{p}$ perpendicular and parallel to the symmetry axis of the target, a is the semi-major axis of ellipsoidal cross section, ϵ is the eccentricity, v is the volume, and

$$f(x) = 3[\sin(x) - x\cos(x)]/x^3$$

The electrostatic polarization matrix is also well known, and its elements for a prolate spheroid are

$$a_{TM} = \frac{1}{\{m^2 - \delta(m^2-1)[(1-\delta^2)\coth^{-1}\delta + \delta]\}}$$

$$a_{TE} = \frac{2}{\{2 + \delta(m^2-1)[(1-\delta^2)\coth^{-1}\delta + \delta]\}} \tag{17}$$

For an oblate spheroid, the elements are

$$a_{TM} = \frac{1}{\{m^2 - \delta(m^2-1)[(1+\delta^2)\coth^{-1}\delta - \delta]\}} \tag{18}$$

$$a_{TE} = \frac{1}{\{2 - \delta(m^2-1)[(1+\delta^2)\cot^{-1}\delta - \delta]\}}$$

where $\delta = \frac{1}{\varepsilon}$. The scattering amplitudes calculated are

$$I_1 = \frac{k_o^2 r^2}{E_o^2}\left|\vec{E}_{sc}\right|^2_{\psi=0°} \quad ; \quad I_2 = \frac{k_o^2 r^2}{E_o^2}\left|\vec{E}_{sc}\right|^2_{\psi=90°} \tag{19}$$

where $\vec{E}_{sc}(\vec{r}) = \alpha\vec{E}^{(1)}_{eff}(r) + \alpha^2\vec{E}^{(2)}_{eff}(r)$; $\alpha = \frac{m^2+1}{4}$

The results are compared with the exact calculation of Reference 3 and appear in Reference 4 as Figures 2 through 4 for the respective aspect ratios 1/2, 1 (sphere), and 5 taking the index of refraction m = 1.33. The incident radiation is along the symmetry axis ($\beta/2 = 0$) and $\phi_1 = 0$). The wave number $k_o = 1\ \mu m^{-1}$.

In these three figures, the second order produces at most a 20% correction to the first order and improves agreement with the exact results. The agreement in all these cases is excellent. For the largest spheroid chosen, Figure 3, the quantity $S = k_o\ell(m-1) = 1$ where ℓ is the spheroidal parameter, $\ell = \sqrt{a^2-b^2}$. Convergence will be faster for $S < 1$ and it will be slower for S greater than 1. A rough limit on the useful convergence of the expansion is $S = 2$. It should be noted that this criterion for convergence applies only to the Shifrin technique of starting from the electrostatic limit.

5. COMPARISON OF THE FINITE CYLINDER AND SPHEROID

The amplitudes I_1 and I_2 are evaluated using the electrostatic polarization matrix elements of the short cylinders. These results for the finite dielectric cylinder are plotted in Figures 2 through 4 of Reference 4 on which the values for the spheroids appear. In each case, the aspect ratios and volumes of the cylinder and spheroid are the same. For these cases the direction of incidence is along the symmetry axis, and we note that the cylinder and spheroid give remarkably similar scattering patterns for the aspect ratios 1/2 and 1. On the other hand, the cylinder with aspect ratio 5 scatters more radiation at large scattering angles than its spheroid counterpart. The index of refraction is 1.33 to compare with the results of Reference 3 (as is the selection of scattering amplitudes shown in these figures). The cylindrical results are shown as dashed lines when they are different from the spheroidal results (solid lines). The open circles shown in these figures are exact results. The wavelength of incident radiation is $2\pi\mu m$.

In Figure 2 of Reference 4, an oblate spheroid and cylinder of aspect ratio 1/2 are shown, each with a volume 3.22 μm^3. In the perturbative calculation the second-order correction is generally about 26% for both targets. We see that the scattering pattern for the amplitudes I_1 and I_2 are nearly the same.

Figure 3 of Reference 4 compares the cylinder with a sphere each with volume 4.19μm^3. Here, the second-order correction is generally about 22%, and the results for the cylinder differ noticeably with the sphere at the larger scattering angles.

Figures 4 and 5 of Reference 4 show the respective amplitudes I_1 and I_2 for a prolate spheroid and cylinder of aspect ratio 5. The volume of each target is 4.31μm^3. The second order correction here is about 25%. In these cases, the cylinder scatters light quite differently at the larger scattering angles. A resonance at about 100° appears for the spheroid in the amplitude I_2 but does not appear at all in the corresponding cylinder.

Figure 8 of Reference 4 depicts the amplitude I_1 for incidence perpendicular to the axis of symmetry ($\beta/2 = 90°$, $\phi_i = 0°$). Two targets are shown, one with an aspect ratio of 2 and volume 1.62μm^3, and the other has an aspect ratio of 5 and volume 4.31μm^3. The second-order correction for the first is about 20% and about 26% for the longer target. We note that the results for the cylinder differ appreciably from the corresponding spheroid only for the larger aspect ratio.

5. ANGULAR SCATTERING DISTRIBUTIONS BY LONG COPPER AND BRASS CYLINDERS: EXPERIMENT AND THEORY

Experimental measurements of EM radiation scattered by long copper and brass cylinders were performed in the IR spectra range ($\lambda = 1.06\mu m$). The cylinders were oriented essentially normal to the scattering plane. This work was done at Fairleigh Dickinson University by Tomaselli, Moeller and Colosi. We have taken the results of the measurements and compared them with the theory for infinite tilted cylinders modified for relatively large indices of refraction. The far field scattering of infinite tilted cylinders is given by

$$I_{11} = \frac{2}{k_o \pi r} \left| b_{oI} + 2 \sum_{n=1}^{\infty} b_{nI} \sin(n\theta') \right|^2 \tag{20}$$

$$I_{12} = I_{21} = \frac{2}{k_o \pi r} \left| 2 \sum_{n=1}^{\infty} a_{nI} \sin(n\theta') \right|^2 \tag{21}$$

$$I_{22} = \frac{2}{k_o \pi r} a_{oII} + \left| 2 \sum_{n=1}^{\infty} a_{nII} \cos(n\theta') \right|^2 \tag{22}$$

The first index in I_{ij} refers to the polarization of the incidence light relative to the incident plane, and the second-polarization of the scattered light relative to the scattering plane. For detailed definitions of the incident and the scattering planes, see Reference 9. θ' is the scattering angle and b_{nI} can be reduced to:

$$b_{nI} = \frac{AJ_n(\alpha) + [BJ_n'(\alpha) - m^2CJ_n(\alpha)][-BH_n'(\alpha) - CH_n(\alpha)]}{AH_n(\alpha) + [BH_n'(\alpha) - m^2CH_n(\alpha)][-BH_n'(\alpha) - CH_n(\alpha)]} \tag{23}$$

where $A = \left(\frac{n\ell}{\alpha}\right)^2 h^2(m^2-1)^2 H_n(\alpha)J_n^2(\beta)$; $B = \ell j^2 J_n(\beta)$; $C = \ell^2 jJ_n'(\beta)$;

$h = \sin\phi$; $\ell = \cos\phi$; $j = (m^2-\sin^2\phi)^{1/2}$; $\beta = \frac{j}{\ell}\alpha$

$J_n(\alpha)$ and $H_n(\alpha)$ are the Bessel and Hankel functions of order n; $\alpha = 2\pi a\cos\phi/\lambda$ is the "tilted" size parameter (a is the cylinder radius, λ the incident wavelength and ϕ is the tilting angle); m is the complex refractive index. The infinite sums in equations (20)-(22) can be truncated a few terms after the order exceeds the "tilted" size parameter, since $J_n(\alpha)\to 0$ for $n>\alpha$ (n, α large). For example, it is generally agreed that for $\alpha^2 > 1$ the number of terms in equations (20)-(22) is of the order of $N=1.2\alpha+5$. Therefore, when m is large (i.e., $m > 10$), the argument in $J_n(\beta)$ satisfies for all b_{nI} in (20), $\beta >> n$. Or

$$J_n(\beta) \sim \left(\frac{2}{\pi\beta}\right)^{1/2} [\cos(\beta - \frac{n\pi}{2} - \frac{\pi}{4})][1 + O(|\beta|^{-1})] \tag{24}$$

For copper and brass cylinders $m = 12-60i$ and $5.3-29i$ respectively (see below). It follows that for any size parameter $\alpha = 2\pi a\cos\phi/\lambda$ larger than 1, $\mathrm{Im}(\beta)$ becomes so large that $J_n(\beta)$ cannot be calculated since it contains the term $\exp\{\mathrm{Im}(\beta)\}$. Hence, in order to calculate the scattering functions for those materials, the expression for b_{nI} has to be modified:

Dividing Equation (23) by β^2 we get

$$b_{nI} = \frac{\frac{A}{B^2}J_n(\alpha) + [J_n'(\alpha) - m^2\frac{C}{B}J_n(\alpha)][-H_n'(\alpha) - \frac{C}{B}H_n(\alpha)]}{\frac{A}{B^2}H_n(\alpha) + [H_n'(\alpha) - m^2\frac{C}{B}H_n(\alpha)][-H_n'(\alpha) - \frac{C}{B}H_n(\alpha)]} \tag{25}$$

The ratio C/B is the only term containing $J_n'(\beta)$ and $J_n'(\beta)$:

$$\frac{C}{B} = \frac{\ell J_n'(\beta)}{jJ_n(\beta)} \tag{26}$$

For large values of β, $J_n'(\beta)$ can be approximated to

$$J_n'(\beta) \sim -\left(\frac{2}{\pi\beta}\right)^{1/2} \sin\left(\beta - \frac{n\pi}{2} - \frac{\pi}{4}\right)$$

$$\Rightarrow \frac{C}{B} \sim i\frac{\ell}{j} \qquad (\mathrm{Im}(\beta) < 0)$$

We note that for $n \to \infty$, b_{nI} reduces to the known ratio $b_{nI} \to J_n(\alpha)/H_n(\alpha)$. Similar expressions can be derived for a_{nII}. When the cylinder axis is not perpendicular to the measurement plane (see Section 12), the scattering intensities calculated by Equations (20)-(22) will have their maximal intensities within the envelope of a cone formed around the cylinder axis. In the event that the tilt angle between such a cylinder and the incident direction is $\phi = 0$, the scattering plane will form an angle ϕ_1, relative to the measurement plane.

The comparison between theory and experiment for $\phi_1 = 0$ then becomes dependent on the opening angle of the light source and its cross sectional variation of intensity (usually gaussian). Here, we discuss quantitatively the case of $\phi_1 = 0$ (copper), and qualitatively the scattering from the brass cylinder for which $\phi_1 \neq 0$ but $\phi_1 \lesssim 3°$.

7. OPTICAL CONSTANTS OF TARGET MATERIALS

The optical constants of several metals from infrared to far-infrared wavelengths have recently been tabulated by Ordal, et al[10] Both n and k are rapidly increasing functions of wavelength in the infrared region. For pure copper at 10.6μm, representative values are n = 12 and k = 60. The brass target wire used has a Cu/Zn ratio of 70/30. For metals at low frequencies, the optical constants can be approximated by

$$n \cong k \cong \sqrt{1/(2\omega\varepsilon_o\rho)} \qquad (27)$$

where ρ is the static resistivity, ω is the angular frequency, and ε_o is the permittivity of free space. Since the resistivities of metals and alloys are easily found, we used the above approximation together with the tabulated data for ρ to obtain the optical constants. The results for brass at 10.6μm is n = 5.8 and k = 29.

The experimental data were taken for wires of various sizes. Figures 2a and 3a of Reference 6 represent the angular scattering results from copper of diameter 242μm and brass of diameter 150μm, respectively.

3. RESULTS AND DISCUSSIONS

The theoretical calculations for the copper wire ($a = 121m$) show that the general angular scattering as well as the accurate angular values of the maxima and minima are predictable by means of the infinite theory. This is clearly shown in comparing the experimental with the theoretical results in Figure 2 of Reference 6. The accurate match shows that the experiment was performed in such a way that the scattering plane and the measurement plane coincided to permit the angular measurements in the same relative units. It is important to note that the general behavior is very sensitive to the size parameter and therefore provides an accurate method for the determination of the size of the scatterer. However, the scattering intensities of the different metallic cylinders are relatively insensitive to changes in the refractive index. This suggests that many properties can be approximately derived by inserting $m \gg 1$ in the scattering equations.

In the case of the brass cylinder (the experimental results are given in Figure 3a and the theoretical results in Figure 3b of Reference 6) the scattering angles for which maxima and minima occur can be predicted, but the general behavior of the experiment (a decreasing envelope) is different than the theoretically predicted increasing envelope. However, the theoretical prediction was calculated for a scattering plane that is perpendicular to the cylinder axis. In the event that the wire is not perpendicular to the measurement plane, having an orientation angle of $(\pi/2 - \phi)$, the scattering direction will be tilted relative to the measurement plane with a varying tilt angle against the scattering angle.

As can be seen in Figure 4 of Reference 6, this varying angle reaches its maximum at $\theta = \pi/2$ where it equals ϕ. More specifically, denoting the measured scattering angle by ϕ and the varying tilt angle ϕ', we get

$$\tan \phi' = \sin \theta \tan \phi \tag{28}$$

The larger the angle ϕ' is, the less is the overlap between the scattering plane field at view (FOV) and the measuring plane FOV resulting qualitatively in a general decrease of the scattering intensity with intensity increasing in the interval $0 \leq \theta \leq \pi/2$.

When $\phi = 0$, the scattering angle must also be modified. Denoting the scattering angle in a plane perpendicular to the cylinder by ϕ', the following relations hold (see Figure 4 of Reference 6)

$$\sin \phi' = \sin \theta' \sin \phi , \qquad \sin \theta' = \frac{\cos \phi'}{\cos \phi} \sin \theta$$

As stated in the section describing the experiment, the orientation of the wire is uncertain to within 3°. Thus $\phi \lesssim 3°$, and as $\phi' \lesssim \phi$, the deviation between θ' and θ is less than the accuracy in the measurement of the scattering angle ($= 4.3°$). Therefore, this effect was not included in the calculation.

9. MULTIPLE SCATTERING

As a first step to a more complete description of the multiple scattering process we have undertaken to describe the double scattering process in as complete detail as possible. The geometry of the double scattering process from non-spherical particles is particularly complex, however, once the geometry is worked out, the transformations necessary to consider higher order scattering are of the same form as the double scattering case.

We have treated in detail the double scattering process from infinitely long randomly oriented cylinders. We have used the exact infinite cylinder solutions so that the cylinders may be of arbitrary diameter and arbitrary index of refraction (both real and complex).

The geometry for calculating the backscattering of a lidar signal from an aerosol layer composed of randomly oriented long cylinders is similar to the geometry described in Reference 1. Two FOVs are of interest - the laser FOV containing the illuminated volume and hence the first scatterer and the receiver's FOV containing the second scatterer. As described in Reference 11, the second FOV is assumed to be larger or equal to the laser FOV (see Figure 1).

The aerosol layer is assumed to have a constant number density, its base being 1000m above the lidar. Since the laser pulse width is of the order of 100 nanoseconds the spatial resolution is approximately 15m. Consequently, the optical depth steps were based on the product of the extinction cross-section of a typical scatterer averaged over all possible orientations, and the number density multiplied by 15m. Reference 11 deals with a given size distribution of spherical scatterers. Here, we deal with long cylinders randomly oriented in space but having one given size.

In order to calculate the sum of all possible double scattering events resulting in a simultaneous signal in the receiver, a statistical approach is used.

Two randomly chosen scattering positions inside the cloud [called A (the lower point) and B (the higher point) in the following analysis] are determined by the computer. The first has the constraint of being within the telescope FOV. An additional constraint requires that the sum of the distances from the source to A, A to B, and B to the receiver be constant to within the resolution of the system for simultaneous reception. In each position, it is assumed that all possible orientations can be found; however, each orientation in the first location corresponds to one scattering angle pointing towards the second location. This is due to the fact that the light scattered by a unit length of the cylinder is limited to the surface of a cone based on the assumption mentioned above that the scatterers are effectively infinite cylinders for aspect ratios greater than about 100 (see Reference 3 and the discussion of Reference 5). The scattering events A and B are shown in Figure 2 with these two points chosen at random (with B higher than A by definition). The incident direction is z_o, the first-scattered direction is z_{AB}, and the final scattered direction is $-z_o$. The reference plane is formed by z_o and z_{AB}. The incident wave denoted E_o, and its direction of polarization makes an angle, α, (relative to the reference plane) as seen in Figure 2. The angle between the z_o axis and AB is $2\phi_o$, and we note from figure 2 that

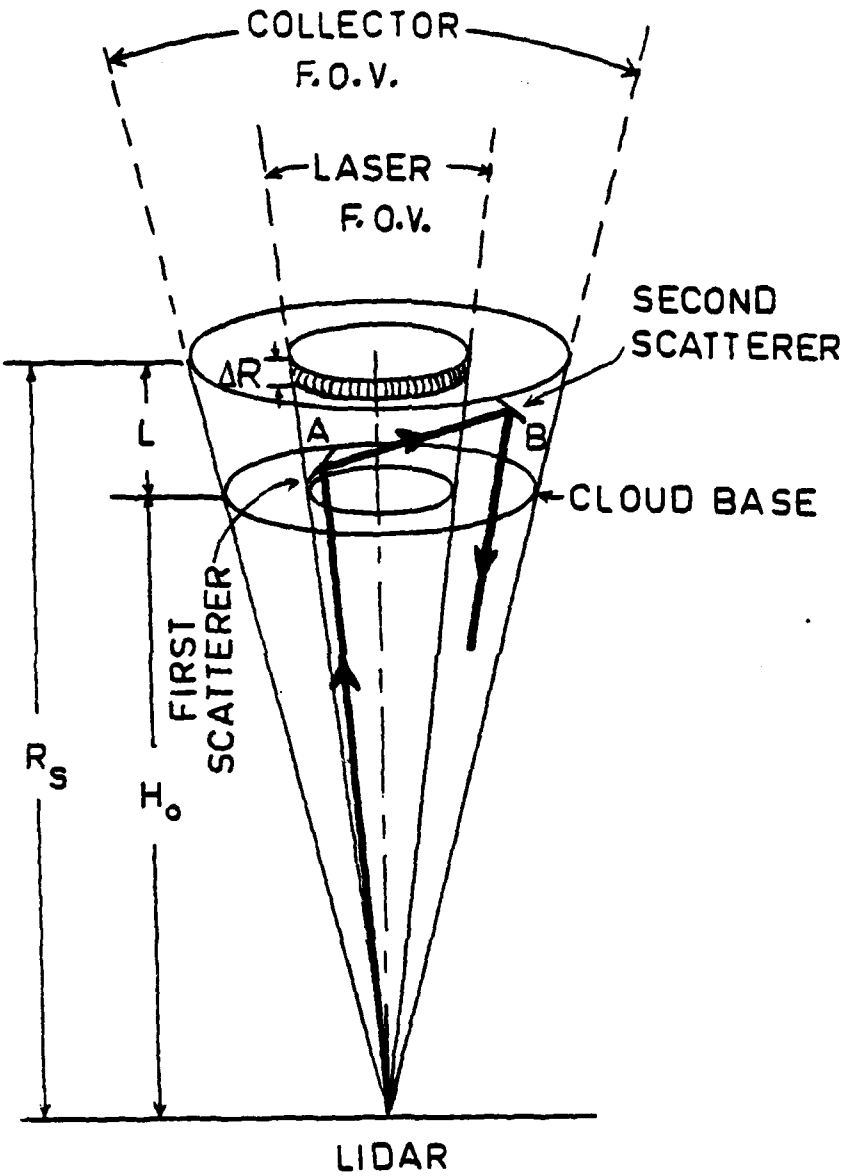

FIGURE 1

TWO OF THE FAMILY OF CONES THAT CORRESPOND TO A GIVEN PAIR OF SCATTERERS.

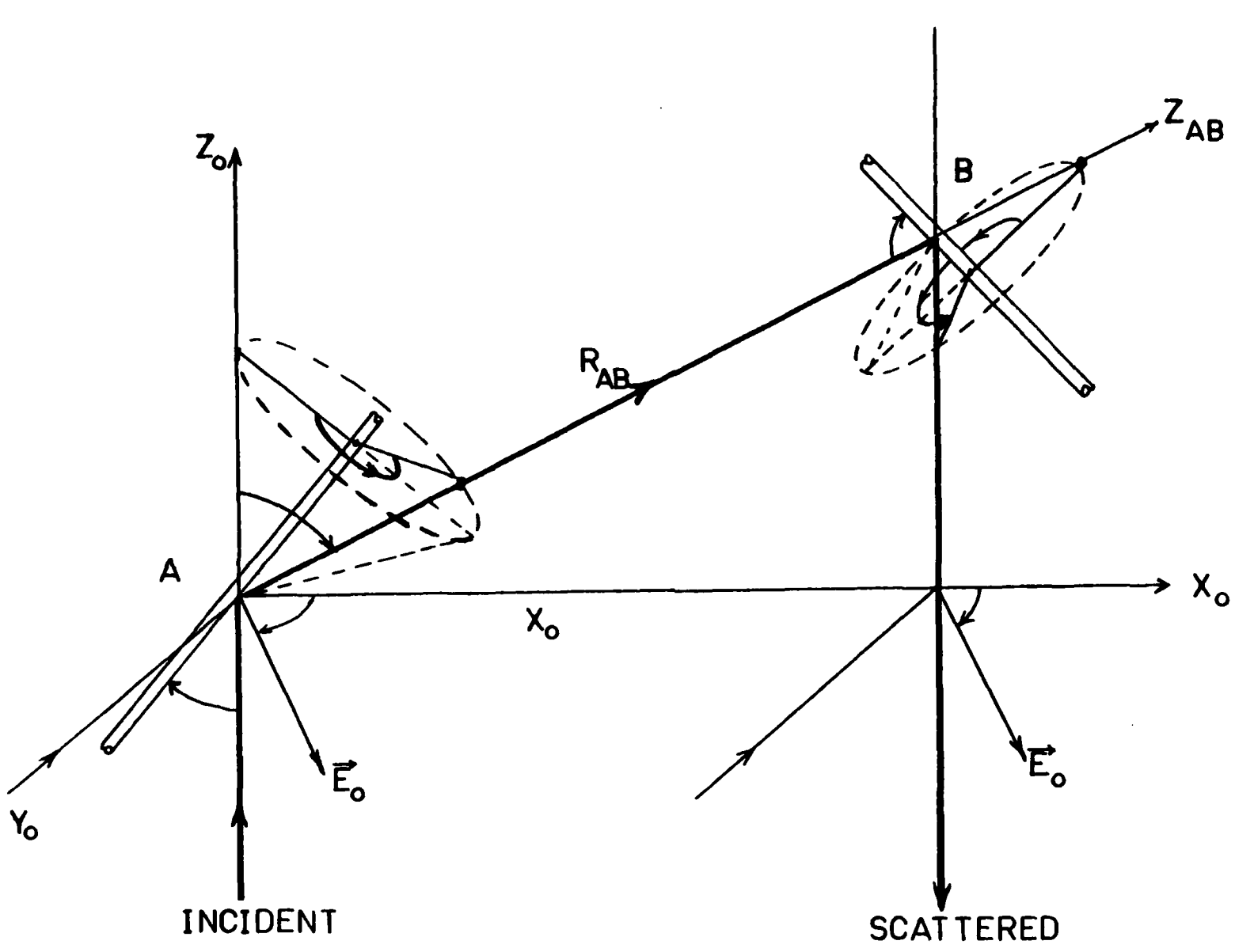

FIGURE 2

DETERMINATION OF THE DOUBLE SCATTERING GEOMETRY AND ORIENTATION ANGLES.

$$\sin 2\phi_o = x_o/R_{AB} \tag{29}$$

with x_o and R_{AB} shown in Figure 2, with $0 \leq \phi_o \leq \pi/2$. We will next show that the tilt angles ϕ_A and ϕ_B of the two cylinders are the only orientational degrees of freedom. Note that only those cones whose tilt angles ϕ_A satisfy $\phi_A \geq \phi_o$ can contribute to the double scattering, as shown in Figure 3.

10. ORIENTATION CONSTRAINTS

We define the tilt angle of a cylinder to be the angle between the axis of the cylinder and the incident direction of the light (the Z_o-axis) - these angles are denoted ϕ_A and ϕ_B for the two cylinders as shown in Figure 2, and $0 \leq \phi \leq \pi$.

First, we note that for the section of a cone shown in Figure 2 with apex angle ϕ_A, $2\phi_o$ the angle between the extreme elements of the section, and θ_A the polar angle at the base of the section

$$\sin \phi_A \sin(\theta_A/2) = \sin \phi_o \tag{30}$$

This relation holds for the first conic section at the point A in Figure 2. The corresponding relation for the conic section at the point B is

$$\sin \phi_B \sin (\theta_B/2) = \cos \phi_o \tag{31}$$

In the following discussion, we use a set of orientation angles α, γ_A, and γ_B. All of these are measured by a counterclockwise rotation from the reference plane. In Figure 4a, the unit vector $\vec{A}$ follows the direction of the axis of the cylinder at point A with its origin at point A. The unit vector $\vec{B}$ follows the direction of axis z_{AB}. Using the frame of reference x_o, y_o, z_o, shown in the figure, we have the following representations:

$$\vec{A} = \sin \phi_A \cos \gamma_A \hat{i}_o + \sin \phi_A \sin \gamma_A \hat{j}_o + \cos \phi_A \hat{k}_o$$

$$\vec{B} = \sin 2\phi_o \hat{i}_o + \cos 2\phi_o \hat{k}_o$$

The scalar product then yields

$$\cot \phi_A = \sin 2\phi_o \cos \gamma_A + \cot \phi_A \cos 2\phi_o$$

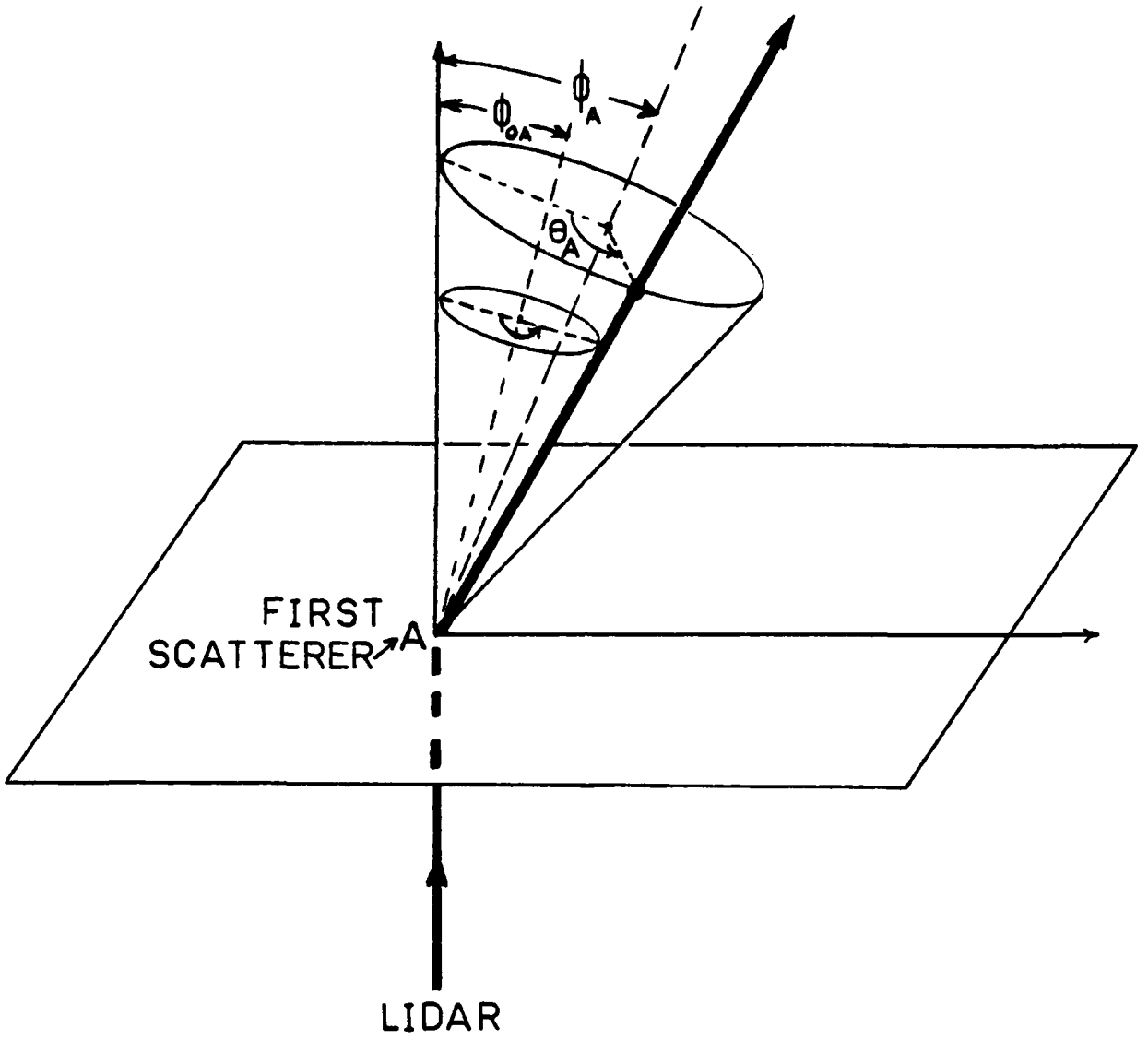

FIGURE 3

DETERMINATION OF THE ORIENTATION OF THE INCIDENT AND SCATTERING PLANES FROM THE FIRST SCATTERER TO POINT A.

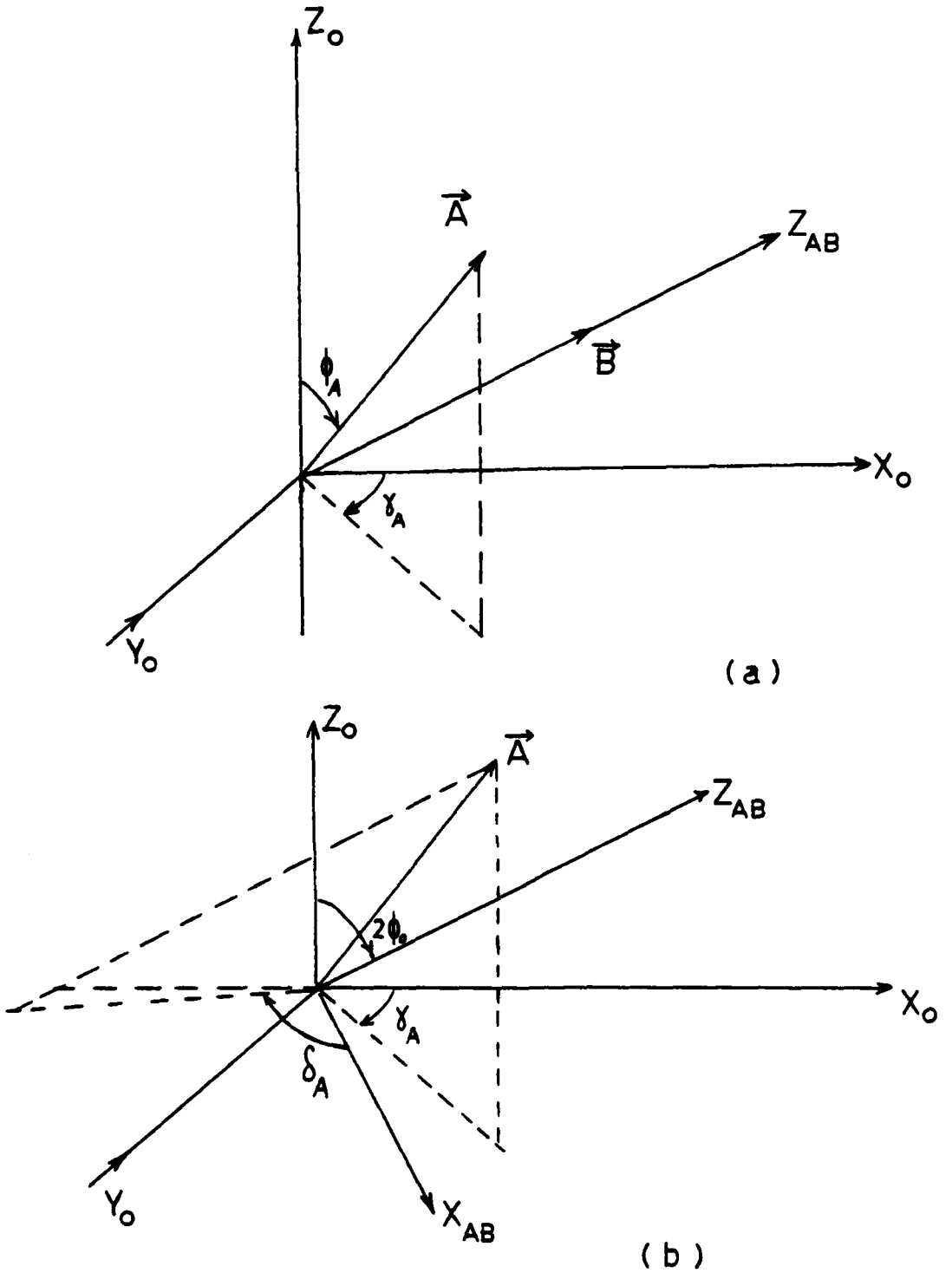

FIGURE 4

GEOMETRY OF THE SECOND SCATTERING AT THE POINT B.

$$\cot \phi_A = \cot \phi_o \cos \gamma_A \tag{32}$$

(Note that $0 \leq \gamma \leq \pi$, and since $\cot \phi_o > 0$, when $\gamma_A \geq \pi/2$ then $\phi_A \geq \pi/2$. Therefore, of the three orientation angles for the first scattering event (ϕ the tilt angle for the cylinder, θ the scattering angle, and γ_A the azimuthal angle of the cylinder axis as shown in Figure 4), there is only one that is independent by the relationships of Equations (30) and (32). Similar results hold for the second cylinder.

Two additional angles are required to describe the double scattering - angle between the first scattering plane and the incidence plane for the second scattering, and the angle between the second scattering plane and the direction of initial polarization. These angles are easily determined in terms of the orientation angles already discussed by first determining the orientations of these scattering planes relative to the reference plane.

In Figure 4b, the angle γ_A is the angle between the x_o axis in the reference plane and the first incidence plane (the first incidence plane is formed by the incident direction and the cylinder axis). We have already represented the unit vector A that is along the axis of the first cylinder in terms of the frame x_o, y_o, z_o, and it follows from this that the azimuthal angle γ_A can be determined from the ratio

$$\cot \gamma_A = A_{x_o}/A_{y_o}$$

The angle δ_A is the corresponding azimuthal angle in the frame x_{AB}, y_o, z_{AB}, and hence satisfies a similar expression in this new frame (see Figure 4b). These two frames of reference are related by a counterclockwise rotation of x_o, y_o, z_o through the angle $2\phi_o$ about the y_o axis:

$$\begin{pmatrix} A_{XAB} \\ A_{Y_o} \\ A_{ZAB} \end{pmatrix} = \begin{pmatrix} \cos 2\phi_o & 0 & -\sin 2\phi_o \\ 0 & 1 & 0 \\ \sin 2\phi_o & 0 & \cos 2\phi_o \end{pmatrix} \begin{pmatrix} \sin \phi_A & \cos \gamma_A \\ \sin \phi_A & \sin \gamma_A \\ & \cos \phi_A \end{pmatrix}$$

It follows that

$$\cot \delta_A = A_{XAB}/A_{Y_o} = \cos 2\phi_o \cot \gamma_A - \cot \phi_A \sin 2\phi_o \csc \gamma_A \tag{33}$$

A similar result holds for the orientation of the second scattering plane (formed by the axis of the second cylinder and the final scattering direction), and this situation is shown in the Figures 5a and 5b.

The next section discusses the scattering intensities. We will need the following angles to complete that discussion.

Angle from the incident polarization direction to the incident plane rotated about z in a counterclockwise direction = $\gamma_A - \alpha$
Angle between the scattering plane to the second incidence plane rotated about $z_{AB} = \gamma_B - \delta_A = \gamma_B - \gamma_A$,
Angle between the second scattering plane and the incident polarization direction rotated about $-z_o = -\alpha - \delta_B = -\alpha - \gamma_B$.
A study of Figures 4 and 5 should clarify these relationships.

II. DOUBLE SCATTERING INTENSITY

The transmitted beam and the double scattering intensities are expressed below in terms of the modified Stokes vector. The transmitted beam is a linearly polarized laser beam with intensity

$$I_o = (I_o, 0, 0, 0).$$

The intensity of the lidar in the plane of polarization is denoted I_o, and the double scattering intensity components $I_{s\parallel}$, $I_{s\perp}$) are expressed relative to I_o. In order to calculate the double scattering intensities in the geometry discussed above, the cloud volumes contained in the FOV angles of the laser and the receiver are divided into n identical sub-volumes. The two scattering events occur in a given cloud layer of depth L, situated at a height H (above the lidar system). The double scattering intensity is calculated by adding the intensities scattered by all possible pairs of the two sub-volumes (one in the transmitter and one in the collector FOV), for which the total path length of the light equals the average path to the top of the cloud layer and back to the lidar system (see Figure 1).

The power scattered at an angle θ_A emerging from a sub-volume ΔV_A, is described by the vector $I_A(\theta_A, \phi_A)$ related to the incident light vector I_o by the scattering matrix for cylinders $P_{cy}(\theta,\phi)$, and a rotational matrix $\mathcal{L}(\gamma_o - d)$ as follows:

$$I_A(\theta_A, \phi_A) = P_{cy}(\theta_A, \phi_A)\,\mathcal{L}(\gamma_A - \alpha) I_o \frac{\Delta V_A}{R_{AB}^2} \exp(-\sigma_{cy}(R_{AB} + R_{OA}) \qquad (35)$$

with σ_{cy} the extinction coefficient. The scattering matrix $P_{cy}(\theta, \phi)$ is

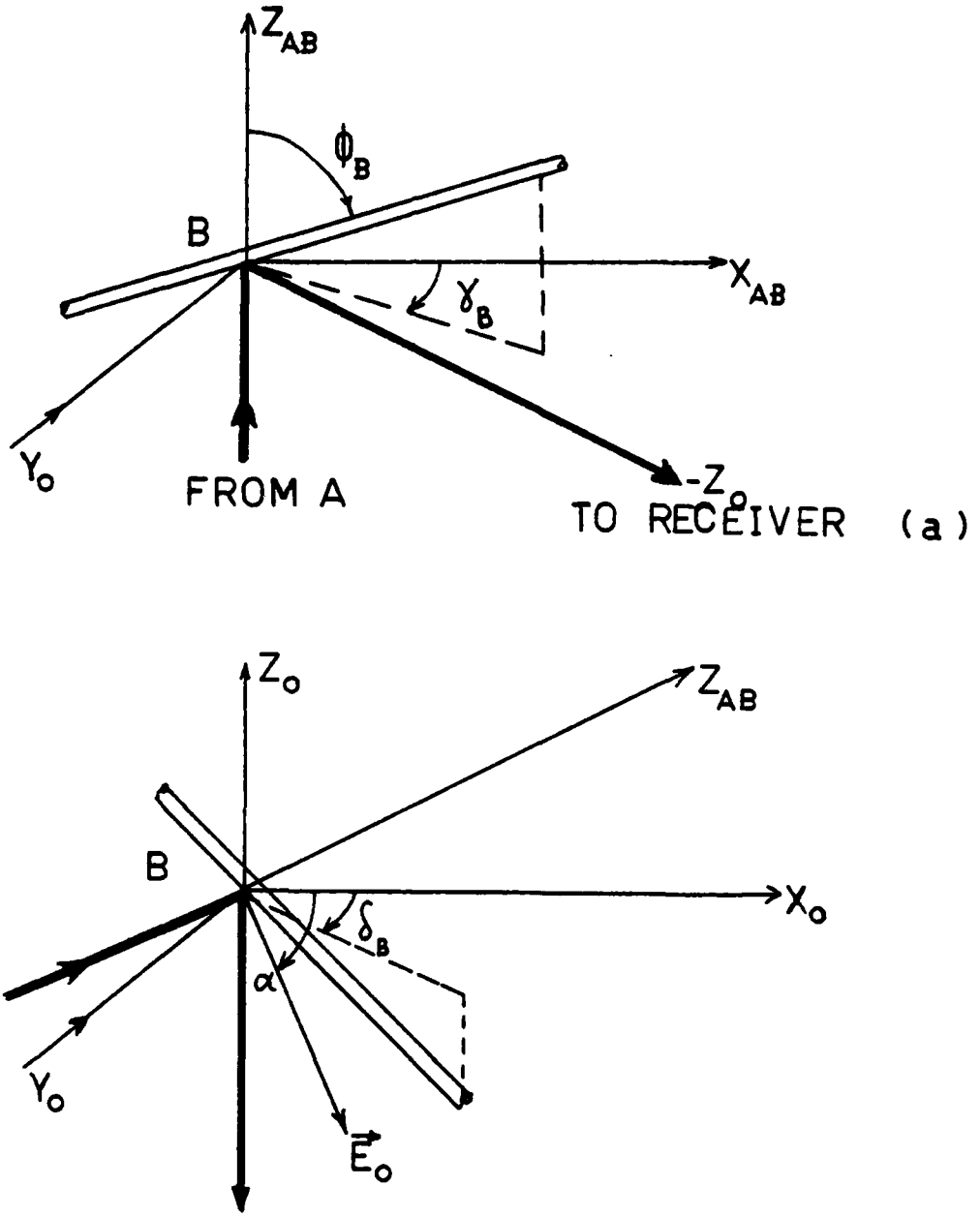

FIGURE 5

GENERAL GEOMETRY FOR DOUBLE SCATTERING OF LIDAR RADIATION FROM A DENSE CLOUD OF PARTICLES.

$$P_{cy}(\theta_A, \phi_A) = \begin{pmatrix} M_2 & M_3 & S_{23} & -D_{23} \\ M_4 & M_1 & S_{41} & -D_{41} \\ 2S_{24} & 2S_{31} & (S_{21} + S_{23}) & (-D_{21} \pm D_{34}) \\ 2D_{24} & 2D_{31} & (D_{21} + D_{24}) & (S_{21} + S_{34}) \end{pmatrix}$$

The matrix elements are related to the cylinder scattering amplitudes A_1, A_2, A_3, A_4 which are functions of the scattering and tilt angles (θ_A, ϕ_A):

$$E_{s\parallel} = A_2 E_{o\parallel} + A_3 E_{o\perp}$$

$$E_{s\perp} = A_4 E_{o\parallel} + A_1 E_{o\perp}$$

where $\vec{E}_o$ and $\vec{E}_s$ are the ingoing and the scattered waves, and

$$M_1 = |A_1|^2 \; ; \quad M_2 = |A_2|^2 \; ; \quad M_3 = |A_3|^2 \; ; \quad M_4 = |A_4|^2$$

$$S_{23} = \mathrm{Re}(A_2 A_3^*) \; ; \quad S_{24} = -S_{23} = -\mathrm{Re}(A_2 A_3^*) \; ; \quad S_{31} = \mathrm{Re}(A_1 A_3^*)$$

$$S_{41} = -S_{31} = -\mathrm{Re}(A_1 A_3^*) \; ; \quad S_{34} = -A_3^2 \; ; \quad S_{21} = \mathrm{Re}(A_1 A_2^*)$$

$$D_{12} = I_m(A_1 A^*_2) \; ; \quad D_{34} = 0 \; ; \quad D_{41} = -D_{31} = \mathrm{Im}(A_1 A_3^*)$$

$$D_{23} = -D_{21} = \mathrm{Im}(A_2 A_3^*)$$

where $A_4 = -A_3$. The rotation matrix $\mathcal{L}(\beta)$ for the modified stokes vector is

$$\mathcal{L}(\beta) = \begin{pmatrix} \cos^2\beta & \sin^2\beta & (1/2)\sin^2\beta & 0 \\ \sin^2\beta & \cos^2\beta & -(1/2)\sin^2\beta & 0 \\ -\sin 2\beta & \sin 2\beta & \cos 2\beta & 0 \\ 0 & 0 & 0 & 1 \end{pmatrix}$$

The pathlength for the lidar system to the first scattering sub-volume is denoted R_{OA}, and the pathlength between the scattering sub-volumes is denoted R_{AB}. Then, using the discussion of the last section on geometry, we can express the intensity of the scattered light after the double scattering events as

$$I_{\bar{s}}(\theta_B, \phi_B, \theta_A, \phi_A) = \sum_i \frac{F\,\Delta V_{Ai}\Delta V_{Bi}}{R_{ABi}^2\, R_{Boi}^2} \exp[-\sigma_{cy}(R_{cy} + R_{ABi})] \tag{36}$$

$$\times \mathcal{L}(-\alpha - \gamma_{Bi}) P_{cy}(\theta_{Bij}\phi_{Bi}) \mathcal{L}(\gamma_{Bi} - \gamma_{Ai}) P_{cy}(\theta_{Aij}\phi_{Ai}) \mathcal{L}(\gamma_{Ai} - \alpha)$$

where σ_{cy} is the extinction coefficient of the randomly oriented cylinders, F is the lidar constant, R_{ABi} is the distance between the two scattering sub-volumes ΔV_{Ai}, and R_{Boi} are the distance between the second scattering volume ΔV_{Bi} and the lidar system.

Note that $R_{ABi} > \Delta R/10$, with ΔR the spatial lidar resolution, therefore no singular points are present. The condition $R_{ABi} < \Delta R/10$ is regarded as single scattering. The pathlength within the cloud that does not include R_{ABi} is denoted R_{cf}. The double scattering geometry is discussed in the previous section. In equation (36) the summation is only over the pairs of sub-volumes obeying

$$R_{oAi} + R_{ABi} + R_{Boi} = 2R_s \tag{37}$$

Here, R_{OA} is the pathlength from the lidar system to the first scattering volume, and R is the height of the top of the cloud layer above the cloud base. Since the size of the sub-volumes should be as small as possible in order to reduce averaging effects, the summation over the number K of all pair (A, B) satisfying equation (37) requires extensive computer time for a case of double scattering. For this reason, a large sample of $g(<< K)$ pairs of points are chosen in six random steps (which determine the coordinates of the scattering points A and B). Each selection places the point A in the first sub-volume and B in the second, and each pair of points replaces a pair of sub-volumes. As the total number of points N (not necessarily satisfying equation (37)) is known, the value of K can be calculated by means of the random program. Each pair of random points is checked to satisfy equation (37) in the following way: the ratio $G = a/g$, where a is the number of pairs contributing to the double scattering process, is recorded and therefore $K = NG$.

In addition to the six random steps which determine the position of scattering cylinders, γ_A and γ_B are randomly chosen from which the scattering and polarization angles are calculated as discussed in the last section. In order to get the double scattering intensity profile from the whole cloud, calculations were performed for several depths in steps corresponding to the spatial resolution of a conventional lidar system. In each step, the whole random process described above was evaluated changing the value of R_s in equation (37).

Since extinction and multiple scattering intensities are strongly dependant on the number density of the scatters, calculations were performed for various relative densities, and the results are presented as intensity profiles as a function of the penetration depth R in the cloud for various number densities (Figures 6 and 7).

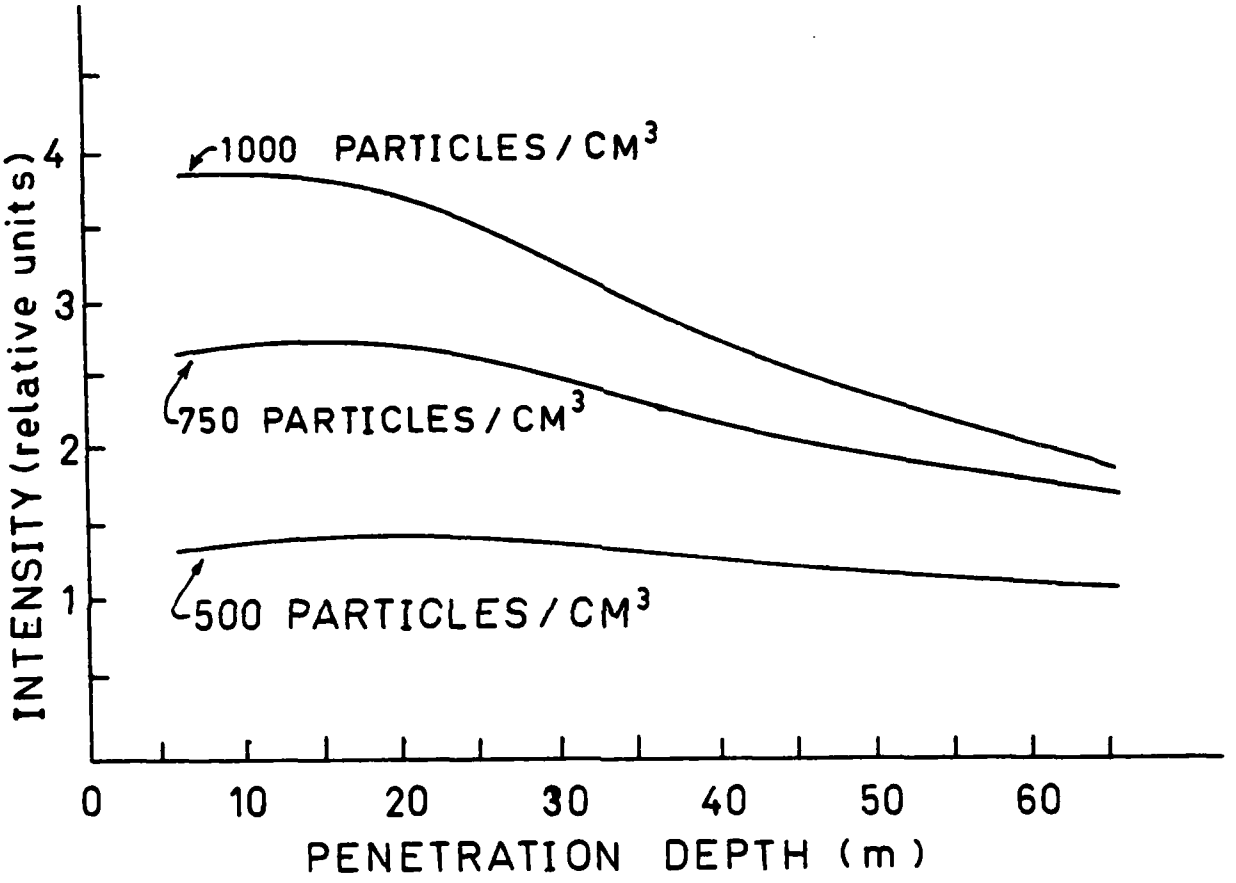

FIGURE 6

DOUBLE SCATTERING INTENSITIES AS A FUNCTION OF PENETRATION DEPTH FOR NUMBER DENSITIES FROM 500 TO 1000 PARTICLES/CM^3.

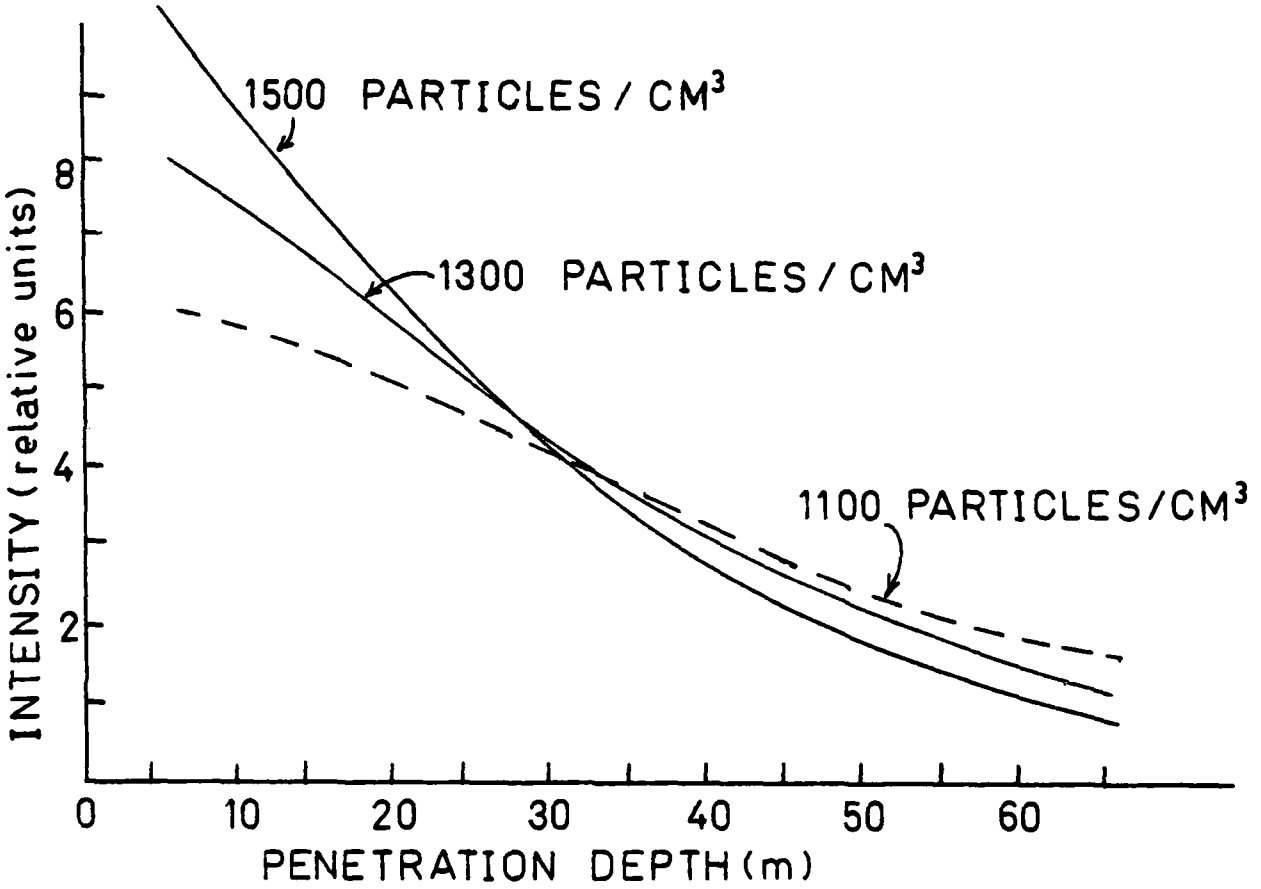

FIGURE 7

DOUBLE SCATTERING INTENSITIES AS A FUNCTION OF PENETRATION DEPTH FOR NUMBER DENSITIES FROM 1100 TO 1500 PARTICLES / CM^3 .

12. DISCUSSION

The double scattering effect of randomly oriented long cylinders was calculated for number densities varying from 5×10^2 to 10^3 and shown in Figure 6 where $0.2 \lesssim \tau \lesssim 0.4$, and for number densities 10^3 to 1.5×10^3 as shown in Figure 7, where $4 \leq \tau \leq 0.6$. In general, the behavior of the double scattering profile as a function of the penetration depth resembles the scattering by dense clouds of spherical particles. As can be seen in Figure 6, the double scattering effect, for relatively low number densities is to produce a maximum scattering layer which approaches the cloud base with an increased value of number density. Single and single plane double scattering intensities are shown in Figure 8 for the number densities 500 to 1000 particle/cm^3. The double scattering readouts are obtained from the results shown in Figure 6.

It is important to emphasize that the geometrical approach discussed here is the first such analysis to appear in literature. Moreover, it can be applied to other non-spherical particles for which the scattering matrices are expressed in terms of a symmetry axis. For example, this treatment is easily extended to finite cylinders by using the matrices developed in Reference 3.

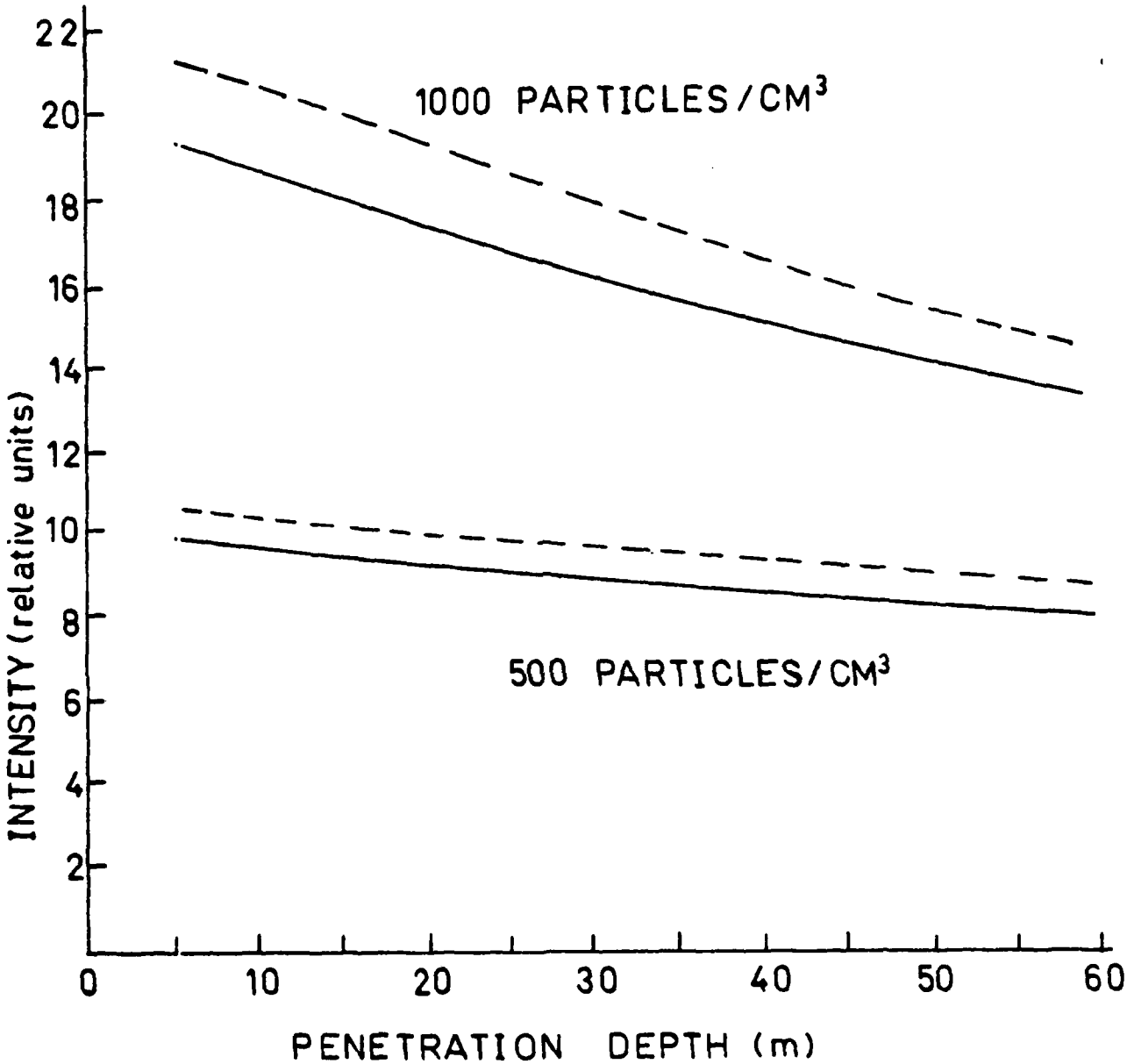

FIGURE 8

_____ SINGLE SCATTERING INTENSITIES

- - - - - SINGLE PLUS DOUBLE SCATTERING INTENSITIES COMPARED FOR NUMBER DENSITIES 500 TO 1000 PARTICLES/CM^3

LITERATURE CITED

1. Acquista, C., "Light Scattering by Tenuous Particles", Appl. Opt. 15, 2932 (1976).

2. Acquista, C., CRCD-CR-DAAK11-80-K.0047,"Scattering Properties of Small Irregular Particulates: Iterative Solutions to Integro-Differential Equations", 6/20/80-1/31/32.

3. Cohen, L. D., Haracz, R. D., Cohen, A. and Acquista, C., "Scattering of Light from Arbitrarily Oriented Finite Cylinders". Appl. Opt. 21, 742 (1983).

4. Haracz, R. D., Cohen, L. D. and Cohen A., "Perturbation Theory for Scattering from Dielectric Spheroids and Short cylinders". Appl. Opt. 23, 436 (1984).

5. Shifrin, K. S., NASA TTF-477 "Scattering of Light in a Turbid Medium". Moscow, 1951, Washington, D.C., 1968.

6. Cohen, A., Cohen, L. D., Haracz, R. D., Tomaselli, V., Colosi, J. and Moeler, K.D., "Angular Scattering Distributions by Long Copper and Brass Cylinders". J. Appl. Phys. 56, 1329 (1984).

7. Van Bladel, J., "Electromagnetic Fields", pp.68-77. McGraw-Hill, New York, 1964.

8. Asano, S. and Yamamoto, G., Appl. Opt. 14, 19 (1975).

9. Cohen A., Opt. Lett. 5, 150 (1980).

10. Ordal, M. A., Long, L. L., Bell, P. J., Bell, S. E., Bell, R. R., Alexander, R. W., Jr., and Ward, C. A., "Optical Properties of the Metals Al, Co, Cu, Au, Fe, Pb, Ni, Pd, Pt, Ti and Wu in the Infrared and Far Infrared", Appl. Opt. 22, 1099 (1983).

11. Cohen, A., Kleiman, M. and Cooney, J., "Lidar Measurements of Rotational Raman and Double Scattering". Appl. Opt. 17, 1905 (1973).

END

FILMED

2-86

DTIC